THE MORPHOLOGIES OF MASSIVE GALAXIES FROM $z \sim 3$—WITNESSING THE TWO CHANNELS OF BULGE GROWTH

M. HUERTAS-COMPANY[1], P. G. PÉREZ-GONZÁLEZ[2,3], S. MEI[1], F. SHANKAR[4], M. BERNARDI[5], E. DADDI[6], G. BARRO[7], G. CABRERA-VIVES[8,9], A. CATTANEO[1], P. DIMAURO[1], AND R. GRAVET[1]

[1] GEPI, Observatoire de Paris, CNRS, Université Paris Diderot, 61, Avenue de l'Observatoire, F-75014 Paris, France
[2] Departamento de Astrofísica, Facultad de CC. Físicas, Universidad Complutense de Madrid, E-28040 Madrid, Spain
[3] Associate Astronomer at Steward Observatory, The University of Arizona, USA
[4] School of Physics and Astronomy, University of Southampton, Southampton SO17 1BJ, UK
[5] Department of Physics and Astronomy, University of Pennsylvania, Philadelphia, PA 19104, USA
[6] Laboratoire AIM, CEA/DSM-CNRS-Université Paris Diderot, Irfu/Service d'Astrophysique, CEA Saclay, Orme des Merisiers, F-91191 Gif-sur-Yvette Cedex, France
[7] University of California, Santa Cruz, 1156 High Street, Santa Cruz, CA 95064, USA
[8] Center for Mathematical Modeling and Department of Computer Science, University of Chile, Santiago, Chile
[9] AURA Observatory in Chile, La Serena, Chile

ABSTRACT

We quantify the morphological evolution of $z \sim 0$ massive galaxies ($M_*/M_\odot \sim 10^{11.2\pm0.3}$) from $z \sim 3$ in the 5 CANDELS fields. The progenitors are selected using abundance matching techniques to account for the mass growth. At $z < 1$, the population matches the massive end of the Hubble sequence, with 30% of pure spheroids, 50% of galaxies with equally dominant disk and bulge components, and 20% of disks. At $z \sim 2-3$ however, there is a majority of irregular systems ($\sim 60\%-70\%$) with still 30% of pure spheroids. We then analyze the stellar populations, star formation rates (SFRs), gas fractions, and structural properties for the different morphologies independently. Our results suggest two distinct channels for the growth of bulges in massive galaxies. Around $\sim 30\%-40\%$ were already bulges at $z \sim 2.5$, with low average SFRs and gas fractions (10%−15%), high Sérsic indices ($n > 3-4$), and small effective radii ($R_e \sim 1$ kpc), pointing toward an even earlier formation through gas-rich mergers or violent disk instabilities. Between $z \sim 2.5$ and $z \sim 0$, they rapidly increase their size by a factor of $\sim 4-5$, are quenched, and slightly increase their Sérsic indices ($n \sim 5$) but their global morphology remains unaltered. The structural evolution is independent of the gas fractions, suggesting that it is driven by ex situ events. The remaining 60% experience a gradual morphological transformation, from clumpy disks to more regular bulge +disk systems, essentially happening at $z > 1$. This results in the growth of a significant bulge component ($n \sim 3$) for 2/3 of the systems, possibly through the migration of clumps, while the remaining 1/3 retain a rather small bulge ($n \sim 1.5-2$). The transition phase between disturbed and relaxed systems and the emergence of the bulge is correlated with a decrease in the star formation activity and the gas fractions, suggesting a *morphological quenching* process as a plausible mechanism for the formation of these bulges.

Key words: galaxies: evolution – galaxies: high-redshift – galaxies: structure

1. INTRODUCTION

In the local universe massive galaxies are characterized by having a dominant early-type, bulge-dominated morphology as well as old stellar populations. They are also confined to tight scaling relations, such as the mass–size relation (e.g., Shen et al. 2003; Bernardi et al. 2014) and the fundamental plane. Understanding the formation and subsequent mass assembly of such systems, however, is still debated in present-day cosmology and is a key milestone toward reaching a complete view of structure formation and the interplay between baryons and their dark-matter hosts. In particular, the actual role played by mergers as compared to in situ processes in shaping spheroids is still unclear, and state-of-the-art semi-analytic models of galaxy formation sometimes offer quite different views (e.g., González et al. 2009; Lapi et al. 2011).

Following the scaling relations of these massive objects across cosmic time is a natural way to better understand how the relations actually emerged and the role played at different cosmic epochs by the different physical mechanisms. As a matter of fact, many works in the last ten years have focused their attention on the evolution of the mass–size relation for a selection of massive galaxies ($\log(M_*/M_\odot) > 10.5$), finding an apparent increase of the zero point of the relation by a factor of a few from $z \sim 3$ (e.g., Daddi et al. 2005; Trujillo et al. 2006; Buitrago et al. 2008; van Dokkum et al. 2008; Damjanov et al. 2011; Cimatti et al. 2012; Newman et al. 2012; Huertas-Company et al. 2013) without significant changes in the slope (e.g., Newman et al. 2012) or the scatter (van der Wel et al. 2014).

Properly interpreting these redshift-dependent evolutionary trends as a progenitor–descendant relation still remains elusive given the continuous mass build-up (e.g., Ilbert et al. 2013; Muzzin et al. 2013), the morphological transformations (e.g., Buitrago et al. 2011), and the evolution of the stellar populations (e.g., Peng et al. 2010) that constitute the galaxies in any given selection (*progenitor bias* effect, e.g., Newman et al. 2012; Carollo et al. 2013; Shankar et al. 2015 and references therein). As a matter of fact, a selection made at fixed stellar mass, as is usually done, will necessarily be *contaminated* by galaxies that grow in mass and will enter any given stellar mass bin. The level of contamination depends on the stellar mass selection. For massive galaxies ($\sim 10^{11} M_\odot$), the fraction of galaxies in the lowest redshift bin that are actually descendants of the galaxies at higher redshift ($z \sim 2$)

is less than 20% (Mundy et al. 2015). Therefore establishing evolutionary links is not straightforward at all. The situation is even worse when passive galaxies are to be considered, since quenching and mass growth both contribute to this progenitor bias effect.

One popular solution has been to study the evolution of the number density of these compact objects (e.g., Trujillo et al. 2011; Cassata et al. 2013; Poggianti et al. 2013; van der Wel et al. 2014; Damjanov et al. 2015), but the results are not always in agreement, especially at low redshifts where *Hubble Space Telescope* (*HST*) surveys probe a small area and also because of the multiple available definitions of *compact galaxies*. As a matter of fact, some works do select only the most massive galaxies ($>10^{11} M_\odot$, e.g., Trujillo et al. 2011) while others select a wider stellar mass bin ($>10^{10.5} M_\odot$, e.g., Poggianti et al. 2013). On the other hand, there are papers using a fixed size threshold (a straight line in the mass–size plane, e.g., Carollo et al. 2013) while others prefer a selection according to the slope of the mass–size relation (e.g., Barro et al. 2013; Cassata et al. 2013; van der Wel et al. 2014). On top of this, other parameters that could bias the results are the environment and also the passive selection criteria (e.g., Valentinuzzi et al. 2010; Poggianti et al. 2013). As a result, several authors do find a steep decrease of their abundances (e.g., Cassata et al. 2013; van der Wel et al. 2014) while others tend to find a rather constant number (e.g., Carollo et al. 2013; Poggianti et al. 2013; Damjanov et al. 2015).

Another option has been proposed based on selecting galaxies at fixed number density (e.g., van Dokkum et al. 2010; Patel et al. 2013 and references therein), i.e., assuming the rank order is preserved at all epochs. This approach also implies some important assumptions such as neglecting the role of mergers or the scatter in the mass accretion histories and it faces the known uncertainties in the evolution of the massive end of the mass function (e.g., Bernardi et al. 2013; Shankar et al. 2014) and the continuous quenching that happens at all cosmic epochs (e.g., Peng et al. 2010). Nevertheless, the latter approach can still provide some broad insights into the expected, average mass growth of galaxies, thus allowing for a basic technique to observationally relate progenitors and descendants. Moreover, the methodology has now been improved by including corrections to the redshift-dependent number densities to account for mergers (Behroozi et al. 2013; Marchesini et al. 2014; Papovich et al. 2014) based on abundance matching. It was also recently stressed that differences in the stellar mass function (SMF) lead to consistent results for the mass growth within ~0.25 dex, at least for galaxies with $\log(M_*/M_\odot) \leqslant 11$ (e.g., Papovich et al. 2014). Globally, these empirical studies based on number conservation procedures tend to agree on a significant structural evolution, and confirm an important size growth of the average population. The growth seems to be driven by the addition of material in the outskirts of the galaxies (e.g., Patel et al. 2013) in what has been called an inside-out growth and interpreted as a minor merger-driven growth through the tidal disruption of small companions falling into the central galaxy (e.g., Naab et al. 2009; Oser et al. 2010; Nipoti et al. 2012; Shankar et al. 2013 and references therein).

Despite the outstanding efforts made so far, it is still challenging to properly follow the evolutionary tracks of especially the most massive galaxies. Number conservation-based approaches map today's red and dead early-type systems

to *progenitors* presenting a variety of morphologies and star formation activities (e.g., van der Wel et al. 2008; van Dokkum et al. 2011; Bruce et al. 2012; Mei et al. 2014; Papovich et al. 2014). It is thus very difficult to interpret the evolution of the overall population as a unique physical mechanism since multiple processes, such as morphological transformations or quenching, can clearly contribute to moving galaxies in the mass–size plane from one redshift bin to another.

By simultaneously following the evolution of the star formation activity (quenching), morphological transformations, and mass build-up along the progenitor tracks identified through number-conserving techniques, one should be able to ideally separate the different contributors to the average structural evolution.

All previous works, however, lack a precise quantification of how the morphologies change and evolve among the progenitors of mainly massive galaxies. The most significant effort has probably been made by Bruce et al. (2012), who made bulge-to-disk decompositions but just on one CANDELS field (UDS) and without quantification of irregularities. Another noticeable effort has been carried out by Mortlock et al. (2013), who in the same UDS CANDELS field visually classified galaxies into discs, ellipticals and peculiar systems. They found significant evolution in the fractions of galaxies at a given visual classification as a function of redshift, though they did not attempt to trace evolutionary tracks among galaxies at different epochs.

This is therefore the main new factor that motivates the present paper, in which we bring into the puzzle of massive galaxy formation detailed *visual*-like morphologies for a large sample of galaxies from all five CANDELS fields. Combined with accurate stellar masses and rest-frame colors as well as optical rest-frame structural parameters from the 3D-*HST* (Brammer et al. 2012) and CANDELS (Grogin et al. 2011; Koekemoer et al. 2011) surveys, we revisit the evolutionary tracks of massive galaxies from $z \sim 3$.

The paper proceeds as follows. In section 2, we describe the data set used as well as the main physical parameters derived (morphologies, structural parameters, star formation rates (SFRs) etc.). In Section 3 we describe the procedure to select the main progenitors and from Section 4 to Section 6 we describe the main results, namely the evolution of the morphologies, structures, and star formation properties. These results are discussed in Section 7 and we provide a summary in Section 8.

Throughout the paper, we adopt a flat cosmology with $\Omega_M = 0.3$, $\Omega_\Lambda = 0.7$, and $H_0 = 70$ km s^{-1} Mpc^{-1} and we use magnitudes in the AB system.

2. DATA SET

2.1. Parent Sample

We select all galaxies in the F160W filter with F160W < 24.5 mag (AB) in the five CANDELS fields (UDS, COSMOS, EGS, GOODS-S, GOODS-N). Our starting-point catalogs are the CANDELS public photometric catalogs for UDS (Galametz et al. 2013) and GOODS-S (Guo et al. 2013), and preliminary CANDELS catalogs were used for COSMOS, EGS, and GOODS-N (CANDELS 2015, private communication). The magnitude cut is required to ensure reliable visual morphologies (Kartaltepe et al. 2014) and structural parameters (van der Wel et al. 2012), which are two key ingredients for the

analysis presented in this work. As discussed in van der Wel et al. (2014), the magnitude cut results in a reasonable mass completeness of $\log(M_*/M_\odot) \sim 10$ at $z \sim 3$, which is well beyond the mass limit required to follow the progenitors of massive galaxies as discussed in the following. Our results should thus not be significantly affected by incompleteness. The median redshift of the sample is $z \sim 1.25$.

2.2. Morphologies

Visual-like morphologies are taken form the deep-learning morphology catalog described in Huertas-Company et al. (2015) on the five CANDELS fields UDS, COSMOS, GOODS-N, GOODS-S, and EGS. The classification mimics the CANDELS visual classification scheme from Kartaltepe et al. (2014), which is currently available in only one field. Morphologies are estimated using ConvNets, a specific artificial neural network topology that is inspired by the biological visual cortex (e.g., Fukushima 1980) and is by far the most powerful image classifier to date. When used for image recognition, convolutional neural networks consist of multiple layers of small neuron collections which look at small portions of the input image, also called receptive fields. The results of these collections are then tiled so that they overlap to obtain a better representation of the original image; this is repeated for every such layer. More details can be found in Huertas-Company et al. (2015, in preparation).

The algorithm is trained on GOODS-S, for which visual classifications are publicly available, and then applied to the other four fields. Following the CANDELS classification scheme, we associate with each galaxy five numbers—f_{sph}, f_{disk}, f_{irr}, f_{PS}, f_{Unc}—measuring the frequencies at which hypothetical classifiers would have flagged the galaxy as having a spheroid, having a disk, presenting an irregularity, being compact or point source, and being unclassifiable/ unclear. As shown in Huertas-Company et al. (2015), ConvNets are able to predict the fractions of votes given a galaxy image with a bias close to zero and $\sim 10\%-15\%$ scatter. The fraction of misclassifications is less than 1%. We refer the reader to the aforementioned work for more details on how the morphologies are estimated. The important information to keep in mind for this work is that the classification is very close to a purely visual classification. We use only a classification in the H band (F160W) since the differences in the derived (broad) morphologies when using other filters are very small as shown in Kartaltepe et al. (2014).

We are interested in distinguishing bulge and disk growth so we use the five morphology estimators to define five main morphological classes as follows:

1. pure bulges [SPH]: $f_{sph} > 2/3$ AND $f_{disk} < 2/3$ AND $f_{irr} < 1/10$
2. pure disks [DISK]: $f_{sph} < 2/3$ AND $f_{disk} > 2/3$ AND $f_{irr} < 1/10$
3. disk+spheroids [DISKSPH]: $f_{sph} > 2/3$ AND $f_{disk} > 2/3$ AND $f_{irr} < 1/10$
4. irregular disks [DISKIRR]: $f_{disk} > 2/3$ AND $f_{sph} < 2/3$ AND $f_{irr} > 1/10$
5. irregulars/mergers [IRR]: $f_{disk} < 2/3$ AND $f_{sph} < 2/3$ AND $f_{irr} > 1/10$.

The classification accounts for the presence or not of a disk/bulge component as well as asymmetries in the light profile. The thresholds used are somehow arbitrary but have been calibrated through visual inspection to make sure that they result in different morphological classes (see also Kartaltepe et al. 2014). We emphasize that slight changes in the thresholds used to define the classes do not affect the main results of the paper. Figure 1 shows some examples of the morphological classes defined that way. The SPH class contains galaxies fully dominated by the bulge component with little or no disk at all. The DISK class is made of galaxies in which the disk component dominates over the bulge. Between these two classes lies the DISKSPH class, in which we put galaxies with no clear dominant component. Then we distinguish two types of irregulars: DISKIRR, i.e., disk-dominated galaxies with some asymmetric features, and IRR, which are irregular galaxies with no clearly dominant disk component (including mergers). These last two categories do contain all the variety of irregular systems usually observed in the high-redshift universe (e.g., clumpy, chain, taphole etc.). The separation between the last two classes, however, is challenging (even for the human eye), since a diffuse light component can be easily interpreted as a disk. Therefore, even though we will consider the two classes separately in most of the plots, the reader should keep in mind that there can be significant overlap. For the galaxies selected in this work (see section 3), >95% of the population fits in one of the five defined classes. The remaining $\sim 5\%$ contains either galaxies with rather high irregular, spheroid, and disk morphologies simultaneously or unclassifiable objects.

2.3. Stellar Masses and SFRs

Photometric redshifts, stellar masses, and SFRs are estimated from spectral energy distribution (SED) modeling as described in previous works by Wuyts et al. (2011, 2012) and Barro et al. (2013, 2014). We describe here the basic procedure and refer the reader to these works for more details. Photometric redshifts are estimated from a variety of different codes available in the literature, which are then combined to improve the individual performance. The technique is fully described in Dahlen et al. (2013). Based on the best available redshifts (spectroscopic or photometric) we then estimate stellar masses and UV-based SFRs using FAST (Kriek et al. 2009), assuming Bruzual & Charlot (2003) models, a Chabrier (2003) IMF, solar metallicity, exponentially declining star formation histories, and a Calzetti et al. (2000) extinction law. Rest-frame magnitudes (U, V, J) based on the best-fit redshifts and stellar templates were computed using EAZY (Brammer et al. 2008).

The final SFR used in this work combines IR-based and UV-based (from SED fitting) SFRs as described in Barro et al. (2011a, 2011b, 2014). The method essentially relies on IR-based SFR estimates for galaxies detected at mid- to far-IR wavelengths, and SED-modeled SFRs for the rest. For IR-detected galaxies the total SFRs, SFRIR+UV, are computed from a combination of IR and rest-frame UV luminosities (uncorrected for extinction) following Kennicutt (1998) and Bell et al. (2005):

$$SFR_{UV+IR} = 1.09 \times 10^{-10} \left(L_{IR} + 3.3 L_{2800} \right) \left[M_\odot \, \mathrm{yr}^{-1} \right]. \quad (1)$$
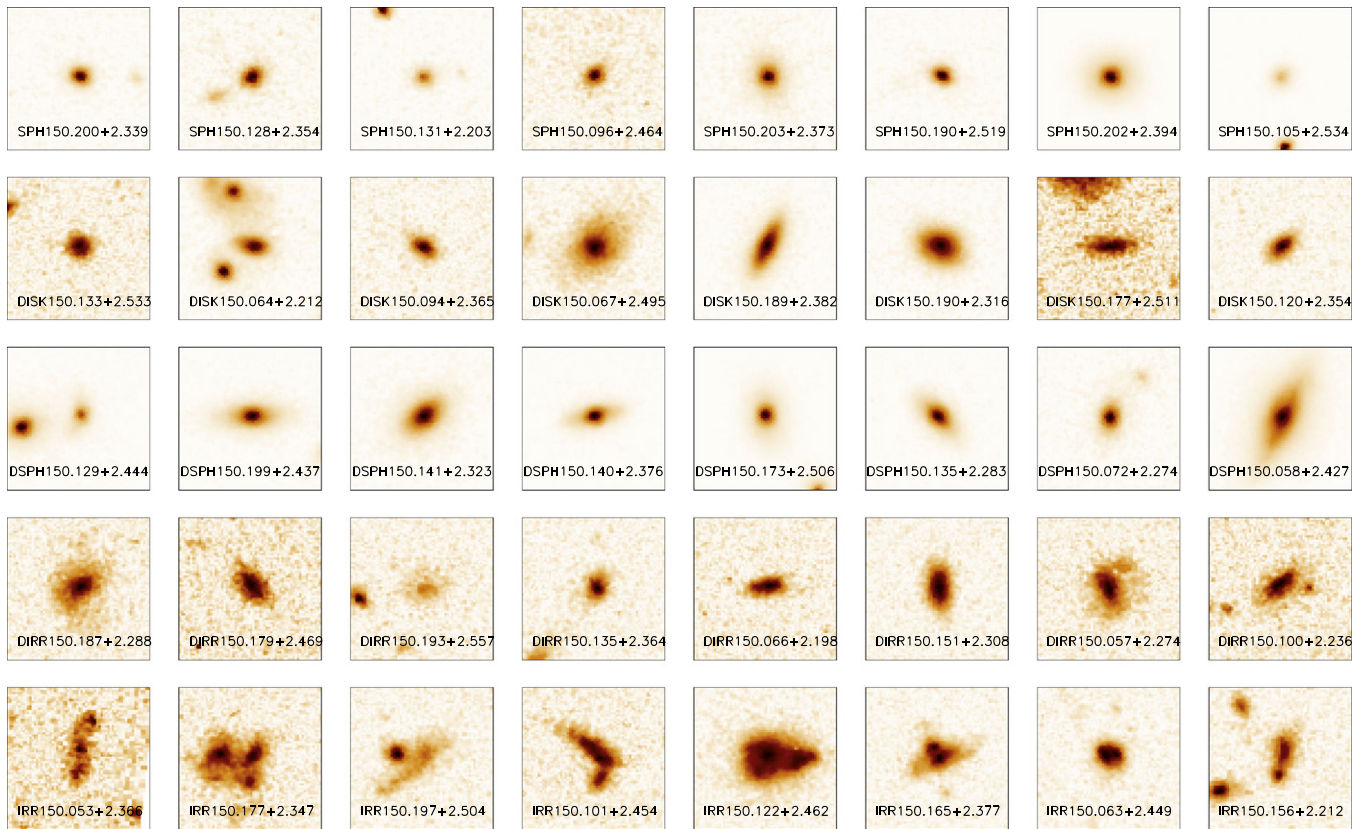
Figure 1. Example stamps of the different morphological types defined in this work from the COSMOS field. From top to bottom: spheroids, disks, disk+spheroids, asymmetric disks, and irregulars. Coordinates are indicated in each postage stamp.

2.4. Structural Properties

Structural properties (effective radii, Sérsic indices, and axis ratios) are taken from the public catalog released in van der Wel et al. (2012). Single Sérsic 2D fits were performed to galaxies in CANDELS in the three infrared filters ($f105$, $f125$, $f160$) using galfit (Peng et al. 2002). The typical uncertainty on the parameters is less than 20% for the magnitude cut applied in this work, as clearly shown in van der Wel et al. (2012). Bernardi et al. (2014) showed, however, that the total light profiles and sizes of massive galaxies at $z \sim 0$ can be significantly affected by the background estimates. We do not expect a major impact of this effect in our sample at higher redshift though, where the contribution of the diffuse light around massive galaxies is less important. van der Wel et al. (2014) applied some corrections to the effective radii of passive and star-forming galaxies to measure them in a unique rest-frame band of 5000 Å. Given that the corrections are very small and have little effect on the final measured structural evolution as discussed in the aforementioned work, we use here for simplicity the closest filter to the optical rest-frame band as done by Newman et al. (2012).

3. SELECTING THE PROGENITORS OF MASSIVE GALAXIES

One key issue when one tries to infer the evolution of individual galaxies is to actually link progenitors and descendants without being strongly affected by progenitor bias (e.g., Carollo et al. 2013; Sonnenfeld et al. 2014; Shankar et al. 2015). The SMF is known to significantly evolve from $z \sim 3-4$ (e.g., Pérez-González et al. 2008; Ilbert et al. 2013;

Muzzin et al. 2013) so a selection at fixed stellar mass will clearly be affected by new galaxies kicking in at lower redshifts, as widely discussed in the recent literature. Also, a selection of only passive galaxies will be affected by the continuous quenching at all cosmic epochs. An alternative that is rapidly becoming very popular in the community is a selection at fixed number density (e.g., van Dokkum et al. 2010; Bezanson et al. 2011; Conselice et al. 2013; Patel et al. 2013). At the first level, this selection assumes that the ranking of galaxies is preserved at all redshifts and therefore deliberately ignores the impact of mergers and the scatter in the mass accretion histories (Behroozi et al. 2013) that can lead to errors in the stellar mass growth of $d(\log M_*)/dz \sim 0.16$ dex (see also Leja et al. 2013 for a comparison with predictions of a semi-analytical model leading to similar conclusions). To overcome this issue, Behroozi et al. (2013) used abundance matching techniques to track the evolution of galaxies within their dark-matter haloes and apply a correction to this simple assumption. The model therefore accounts for number density evolution and is the one adopted in this work. Figure 2 shows the stellar mass growth track for the progenitors of $\sim 10^{11.2} M_\odot$ galaxies from $z \sim 4$ from the model of Behroozi et al. (2013), assuming the SMFs of Baldry et al. (2008), Moustakas et al. (2013), Pérez-González et al. (2008), Mortlock et al. (2011), and Marchesini et al. (2009, 2010). As recently shown by Papovich et al. (2014), using different abundance matching assumptions (e.g., Moster et al. 2013) or different measured SMFs leads to consistent results for the mass growth within ~ 0.25 dex. The figure confirms that massive galaxies grow by a factor of 2 in stellar mass from $z \sim 2$ and a factor of ~ 5 from
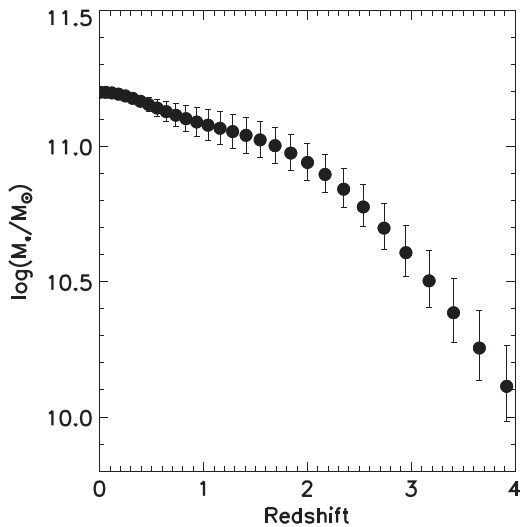
Figure 2. Predicted mass growth of the progenitors of $\log(M_*/M_\odot) = 11.2$ galaxies from $z \sim 4$ from the model of Behroozi et al. (2013). Error bars show the errors on the median mass at a given redshift.

$z \sim 3$, so that the typical stellar mass of the progenitors of $\sim 10^{11.2} M_*/M_\odot$ galaxies is $10^{10.5} M_\odot$ at $z \sim 3$ and $10^{10.0} M_\odot$ at $z \sim 4$. This mass growth track includes mergers, which occur at a rate of ~ 1.2 major (1:4) mergers/galaxy between $z \sim 3$ and $z \sim 0.5$ (see section 7.3 for a detailed discussion of the effect of mergers). Since our sample is mass-complete down to 10.0 from $z \sim 3$, a selection along the progenitors should not be affected by incompleteness. As described in Patel et al. (2013), we select galaxies along the growth track by picking galaxies in a given redshift bin within a narrow stellar mass bin of 0.3 dex around the corresponding mass for that redshift. As also discussed in Papovich et al. (2014), this stellar mass bin is a reasonable trade-off to account for the different predictions of different methods/SMFs and the scatter in the mass accretion histories. Table 1 summarizes the main properties of the selected sample at different redshifts. The redshift bins are selected to keep a comparable number of objects in each bin (~ 400, except for the first and last bins) and as a trade-off between comoving volume ($\sim 3 \times 10^5 \, \mathrm{Mpc}^3$) and lookback time ($0.5-1 \, \mathrm{Gyr}$).

4. MORPHOLOGICAL EVOLUTION

Figure 3 shows the evolution of the relative abundance of the different morphological types defined in Section 2.2 selected along the mass growth track from Figure 2 in 0.3 dex bins. The plot confirms the strong morphological evolution experienced by the population of massive galaxies between $z \sim 3$ and $z \sim 1$ essentially (see also, e.g., van Dokkum et al. 2011; Bruce et al. 2012; Mortlock et al. 2013). About 60%−80% of the progenitors of massive galaxies at $z \sim 3$ were irregular disks ($\sim 40\%-50\%$) and mergers/irregulars ($\sim 20\%-30\%$), while the population at $z < 1.0$ consists of 80%−90% pure spheroids and galaxies with a classic bulge+disk structure. Below $z \sim 1$, the well-known massive end of the Hubble sequence seems to be in place in terms of morphological mixing. Figure 4 illustrates this morphological transformation with some example color stamps. Hence, considering all the progenitors of massive galaxies as a homogeneous family of objects when trying to infer their structural evolution necessarily ignores the

striking diversity of morphologies and the effect of morphological transformations.

The inspection of the evolution for each morphology individually reveals some interesting trends. The fraction of *pure* spheroids is in fact roughly constant with redshift and represents about $\sim 30\%$ of the population of massive galaxies at all epochs (only a slight decreasing trend is observed at $z > 2.5$). Most of the evolution is observed in the bulge+disk and the irregular disk populations, which present more or less symmetric trends as clearly shown in the bottom panel of Figure 3. The latter goes from $\sim 60\%$ of the population of massive galaxies at $z \sim 3$ to roughly $\sim 5\%$ at $z \sim 0.2$. This decrease is mirrored by the increase in the disk and bulge+disk populations, which are almost nonexistent at $z = 3$ and represent 50% of the galaxy population at low redshift. These trends suggest that most of the morphological transformations going on in the progenitors of massive galaxies go in just one direction, i.e., from irregular/clumpy disks to more regular bulge+disk galaxies, while the population of pure spheroids remains unaltered from $z \sim 2.5$ and might follow an independent evolutionary track.

The result might be an indication of two independent channels for bulge growth in massive galaxies acting at very different timescales. Around $\sim 30\%$ of the population of massive galaxies at $z \sim 0$ already consisted of bulges at $z \sim 2.5$ with probably an early (*monolithic*) fast collapse. The other half, however, clearly have a disk component and seem to appear gradually from $z \sim 3$ and $z \sim 1$ (~ 3 Gyr) through the morphological transformation of clumpy-irregular disks, possibly through the migration of clumps and stabilization of the disks (e.g., Bournaud et al. 2014).

5. STAR FORMATION

We now explore how the stellar populations, SFRs, and gas fractions evolve for each morphological type. Figures 5 and 6 show the evolution of the *UVJ* planes for different morphological types. Objects with different morphologies clearly populate different regions of the color–color plane as expected. Disk-dominated galaxies (disks and irregular disks) tend to populate the star-forming region at all redshifts while pure spheroids are more concentrated toward the quiescent zone. Disk+spheroid galaxies lie between these two regions. This confirms that, while a separation between passive and star-forming galaxies, such as that done for example by van der Wel et al. (2014), is clearly correlated with the morphology, it will not result in a clean separation of the morphological types and will mix bulges and disks. This is better seen in the left panel of Figure 7, which shows the quiescent fraction for different morphologies, where quiescent galaxies are selected using the *UVJ* plane (red box in Figures 5 and 6). The average population is clearly quenched between $z \sim 3$ and $z \sim 0.5$ with the quiescent fraction rising from $\sim 20\%$ at $z \sim 3$ to $\sim 80\%$ at $z \sim 0$, in agreement with the findings of Patel et al. (2013) and Papovich et al. (2014). However, 90% of the disks and irregular disks are star-forming at all redshifts and show no significant increase in the number of passive galaxies. In a similar vein, bulge+disk galaxies have a rather constant quiescent fraction at all redshifts, close to 60%. The spheroid population, however, shows a clear increase, going from a passive fraction of 60% at $z \sim 3$ to almost 90% at $z \sim 0$. Given that the number density of spheroids remains roughly constant in the redshift range probed, this trend can be easily interpreted

Table 1
Summary of Selected Objects

Redshift	c. vol. (Mpc³)	Time (Gyr)	$\log(M_*/M_\odot)$	N Total	% SPH	% DISK	% DISKSPH	% DISKIRR	% IRR	% Other
(1)	(2)	(3)	(4)	(5)	(6)	(7)	(8)	(9)	(10)	(11)
$0.10 < z < 0.60$	5.91×10^4	4.27	11.17 ± 0.3	76	34	18	34	1	7	1
$0.60 < z < 1.10$	1.86×10^5	2.31	11.10 ± 0.3	455	28	23	35	5	4	2
$1.10 < z < 1.60$	2.74×10^5	1.36	11.05 ± 0.3	416	29	18	24	14	7	4
$1.60 < z < 2.10$	3.15×10^5	0.87	10.97 ± 0.3	482	30	17	9	25	11	4
$2.10 < z < 2.60$	3.27×10^5	0.59	10.84 ± 0.3	319	26	6	2	31	24	8
$2.60 < z < 3.00$	2.60×10^5	0.35	10.67 ± 0.3	157	14	6	1	41	28	7

Notes. (1) Redshift range, (2) comoving volume probed in the corresponding redshift range considering the CANDELS area, (3) lookback time interval, (4) stellar mass range, (5) total number of objects, (6) number of spheroids, (7) number of disks, (8) number of disk+spheroids, (9) number of irregular disks, (10) number of irregulars, and (11) remaining galaxies which include unclassified, disk+irr+spheroids, and sph+irr.
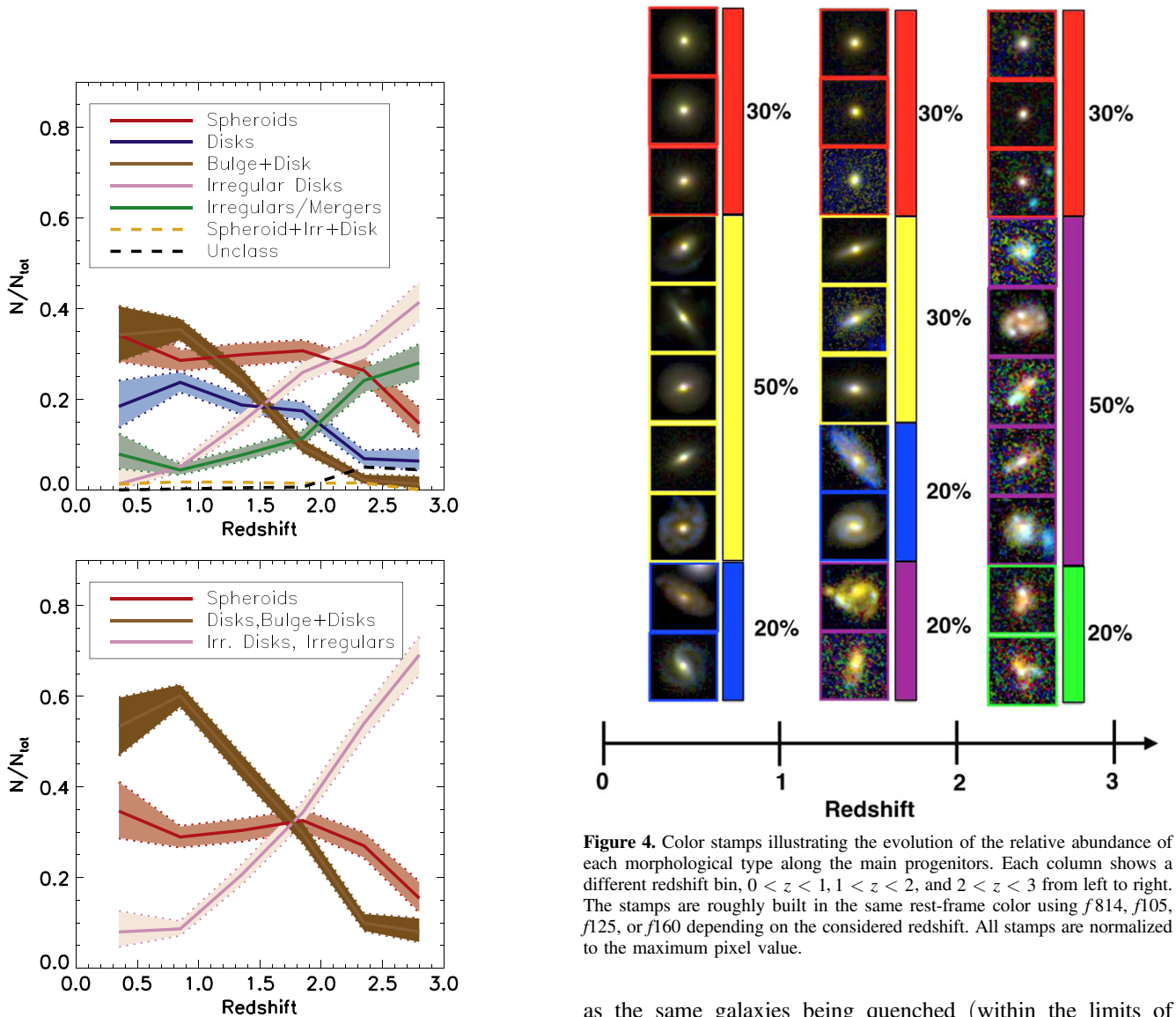

Figure 3. Evolution of the relative abundances of different morphological types as labeled between $z \sim 0$ and $z \sim 4$ along the mass growth tracks from Behroozi et al. (2013) (see text for details). The shaded regions indicate the 1σ error on the fractions computed following Gehrels (1986) (see Section 3 for binomial statistics; see also Mei et al. 2009). The top panel shows all the morphological types defined in Section 2.2. In the bottom panel, all the irregulars are combined into one class and all the *disky* galaxies into another.

Figure 4. Color stamps illustrating the evolution of the relative abundance of each morphological type along the main progenitors. Each column shows a different redshift bin, $0 < z < 1$, $1 < z < 2$, and $2 < z < 3$ from left to right. The stamps are roughly built in the same rest-frame color using $f814$, $f105$, $f125$, or $f160$ depending on the considered redshift. All stamps are normalized to the maximum pixel value.

as the same galaxies being quenched (within the limits of the selection based on abundance matching). The increasing quiescent fraction observed for the overall population could then be explained as a combination of morphological transformations of disk–irregular galaxies becoming disk +spheroids (as suggested by Figure 3) and spheroids being individually quenched.
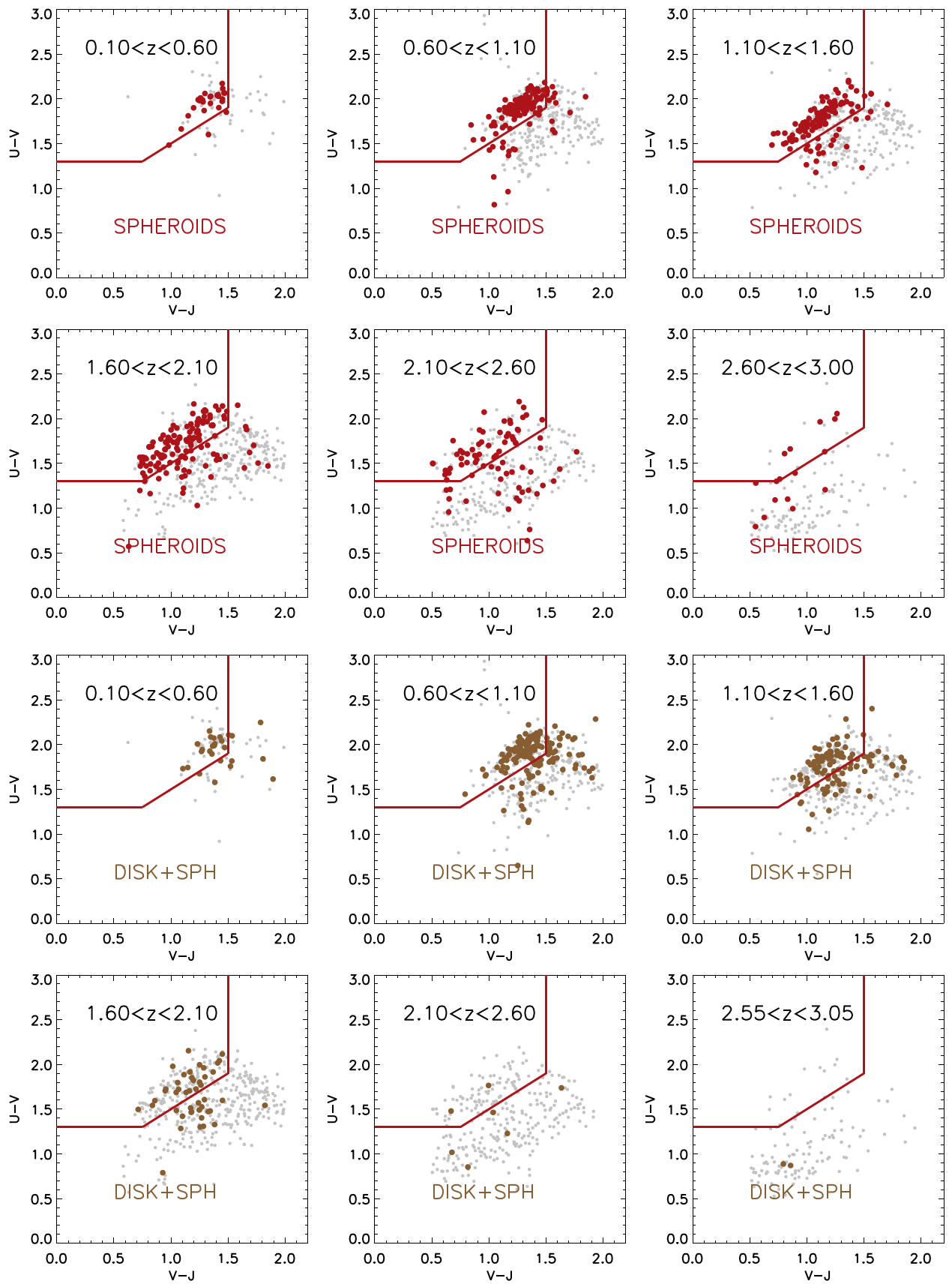
Figure 5. Rest-frame *UVJ* plane for spheroids (top panels) and disk+sph (bottom panels) at different redshifts as labeled. The red lines indicate the quiescent region as defined by Whitaker et al. (2012) and gray points are all galaxies in the corresponding redshift/mass bin.
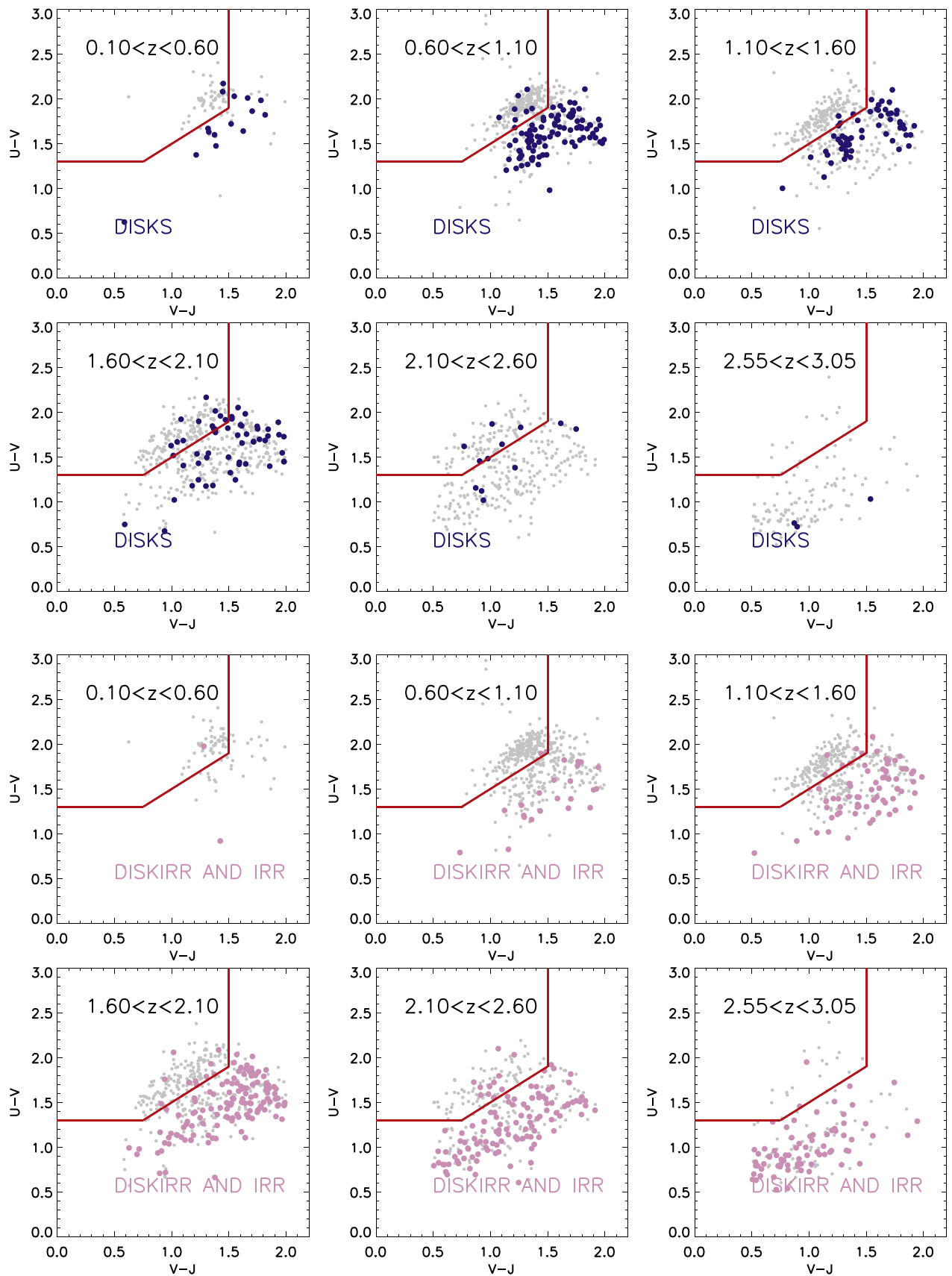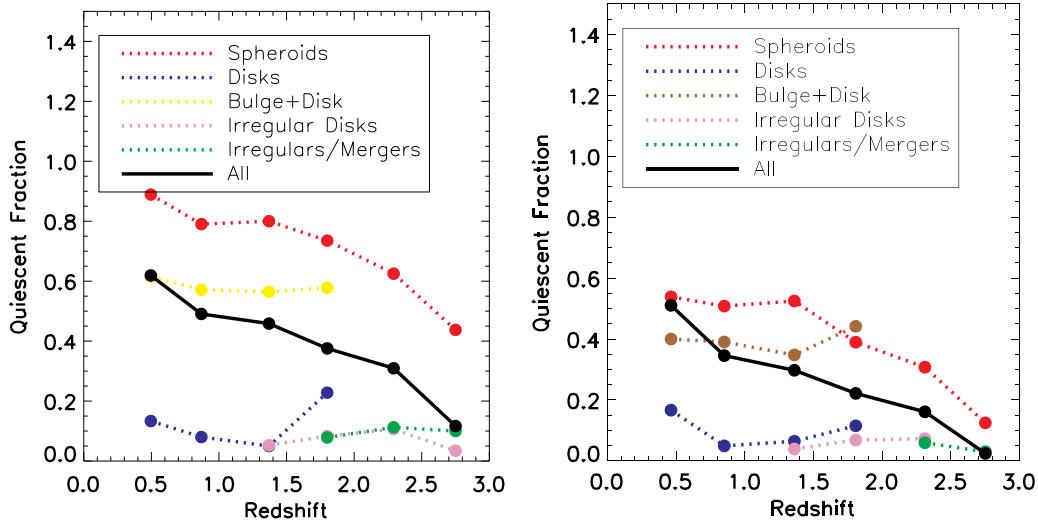
Figure 6. Rest-frame *UVJ* plane for disks (top panels) and disk irregulars (bottom panels) at different redshifts as labeled. The red lines indicate the quiescent region as defined by Whitaker et al. (2012) and gray points are all galaxies in the corresponding redshift/mass bin.

Figure 7. Quiescent fraction as a function of redshift for different morphological types as labeled. In the left panel, the quiescent fraction is computed using the *UVJ* plane while in the right panel a threshold in sSFR ($\log(\text{sSFR}[\text{Gyr}^{-1}]) < -1.5$) is used. The trends are the same, but the absolute number of objects considered as passive changes depending on the definition used.

A similar conclusion arises from Figure 8, in which we plot the median SFR and specific star formation rate (sSFR) for all morphologies. Different morphologies form stars at very different rates at all epochs, ranging from several hundreds of solar masses per year for the irregular and irregular disks to a few tens for spheroids. Generally speaking, objects with a significant bulge component tend to lie below the star formation main sequence at all redshifts (Whitaker et al. 2012 shown with stars in Figure 8). The overall trend (black line in Figure 8), however, is a clear decrease of the SFR irrespective of the morphological type, as predicted by several models (e.g., Dekel & Birnboim 2008; Peng et al. 2010) and in agreement with the evolution of the star formation main sequence (Whitaker et al. 2012).

Spheroids had a modest (compared to the average main sequence at that epoch, i.e., Whitaker et al. 2012) star formation activity already at $z \sim 2-3$ (SFR $\sim 50 M_{\odot}$ yr^{-1}), suggesting again that the formation of their stellar content occurred at earlier epochs and that they are in the process of quenching, i.e., their SFR at $z \sim 0.5$ is almost 0. We do observe, however, a significant increase of the average sSFR, and above $z \sim 2$ it becomes larger than the threshold used by Barro et al. (2013) to define quiescent galaxies ($\log(\text{sSFR}[\text{Gyr}^{-1}]) = -0.5$). This increase is also accompanied by an increase in the scatter as also shown in Figure 8. At $z > 2$, a significant fraction of spheroids are therefore actively forming stars, at similar rates to $z \sim 1$ main sequence disks (see also Barro et al. 2013).

Clumpy disks have rather high SFRs ($>100 M_{\odot}$ yr^{-1}) at all epochs in which they are still abundant ($z > 1-1.5$) as well as disk-dominated galaxies, roughly lying in the main sequence. Bulge+disk galaxies form roughly $50 M_{\odot}$ yr^{-1}, departing from the star formation main sequence. This suggests that, while the transition from irregular disks to disk-dominated systems appears to be smooth without a big impact on the star formation activity, the morphological transformation between irregular and bulge+disk (i.e., the emergence of the bulge component) has to be accompanied by a decrease of their star formation activity and a departure from the main sequence. In other words, the emergence of the bulge and the stabilization of

the disk in these objects tends to decrease their SFR significantly. This behavior is in line with the predictions of several numerical simulations (e.g., Martig et al. 2009) which predict that the growth of a bulge in a turbulent disk can be sufficient to stabilize the gas disk and quench star formation (*morphological quenching*). Another possibility is that the quenching which seems to follow the growth of the bulge is driven by the effects of a supermassive black hole (SMBH) in the growing bulge (e.g., Silk & Rees 1998; Granato et al. 2004).

To follow up on this idea, we look at the gas fractions through the existing correlation between the surface density of the SFR and the cold gas using the Kennicut–Schmidt law (Schmidt 1959; Kennicutt 1998). As done in Conselice et al. (2013) and Papovich et al. (2014), we use the following relation to infer gas masses:

$$\frac{M_{\text{gas}}}{6.8 \times 10^8 M_{\odot}} = \left(\frac{\text{SFR}}{1 M_{\odot} \text{ yr}^{-1}}\right)^{5/7} \left(\frac{R_{\text{e}}}{1 \text{ kpc}}\right)^{4/7}, \qquad (2)$$

which is then used to estimate the gas fraction as

$$f_{\text{gas}} = \frac{M_{\text{gas}}}{M_{\text{gas}} + M_{*}}. \qquad (3)$$

Figure 9 shows the evolution of the inferred gas fractions for different morphologies. The average gas fraction decreases monotonically with redshift from a value of $\sim 60\%$ to $\sim 20\%$ at $z \sim 0.5$ as already reported in Papovich et al. (2014) for a slightly less massive sample. The trends differ significantly for different morphologies though. Spheroids tend to have low gas fraction ($\sim 10\%$), at least from $z \sim 2$, while irregulars and disk+irregulars keep high gas mass fractions ($50\%-60\%$).

The increase in the gas fraction of spheroids at $z > 2.5$, even with the large uncertainties, is in line with the idea of these objects rapidly assembling at these epochs and consuming their gas reservoirs. On the other hand, the decrease in the gas content in disk galaxies is again tightly linked with the emergence of the bulge component. While the decrease is rather smooth when no significant bulge is built, it becomes
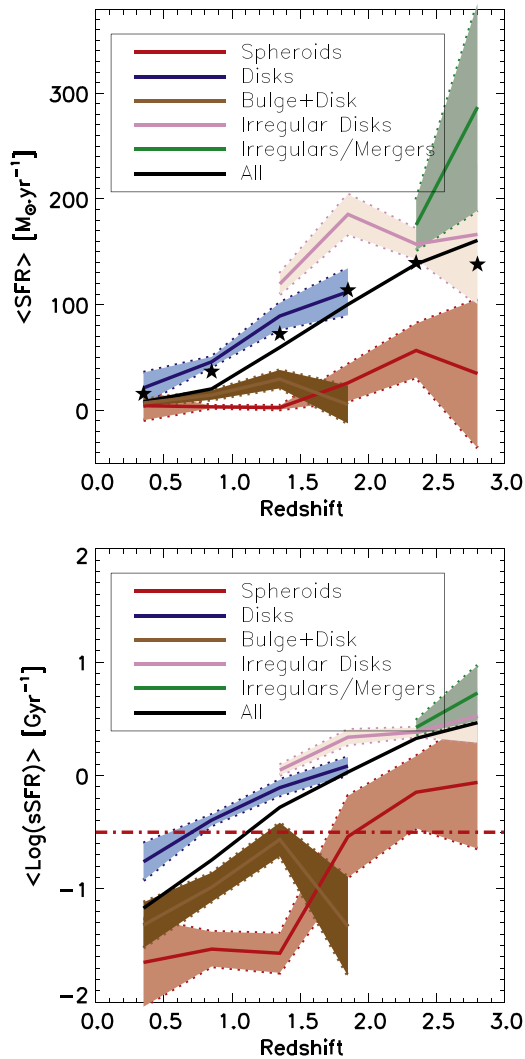
Figure 8. Median SFR (top) and sSFR (bottom) for different morphological types. Red: spheroids; brown: disk+sph; blue: disks; violet: disk+irr; green: irr. The shaded regions show the 1σ uncertainty estimated through bootstrapping. Black stars in the top panel show the position of main sequence galaxies at a given redshift according to the measurement of Whitaker et al. (2012). The red dashed–dotted line in the bottom panel shows the limit used by Barro et al. (2013) to define star-forming and quiescent galaxies. We only plot morphologies that represent at least 10% of the total population at a given epoch.

more dramatic for galaxies with a more predominant bulge (decreasing from ~40% to ~20%).

6. STRUCTURE

We now move on to the study of the evolution of the structural properties of the different morphological types. Figure 10 shows the evolution of the effective radii, Sérsic indices, and axis ratios. There is an average size increase by a factor of ~2 from $z \sim 3$, as already pointed out in many works (e.g., Daddi et al. 2005; Trujillo et al. 2006; Buitrago et al. 2008; van Dokkum et al. 2008; Damjanov et al. 2011; Cimatti et al. 2012; Newman et al. 2012; Huertas-Company et al. 2013). We do clearly find two regimes in the size growth as also discussed by Patel et al. (2013) for a similar selection. From $z \sim 3$ to $z \sim 1.5$, the average size of the whole population remains roughly constant and starts a sharp increase from $z \sim 1.5$ to $z \sim 0$. Recall that this differs from other works
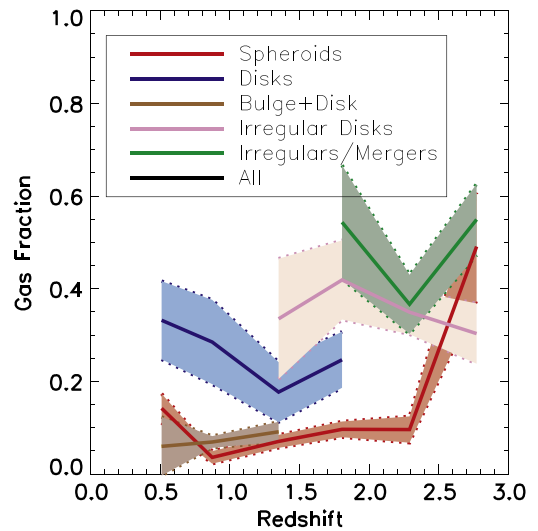

Figure 9. Median gas fractions for different morphologies. The black solid line show the average population while the different colors show different morphologies: red: spheroids, brown: disk+sph, blue: disks, violet: disk irregulars, green: irregulars. The shaded regions show the 1σ errors on the mean estimated through bootstrapping. We only plot morphologies that represent at least 10% of the total population at a given epoch.

selected at fixed stellar mass (e.g., Newman et al. 2012) because the selection is different. By adding the information on the morphological evolution discussed in Section 2.2, these two phases in the structural evolution are better explained. From $z \sim 3$ to $z \sim 1.5$ there is a rapid morphological transformation of irregular disks into bulge+disk systems. Even though irregular disks are rapidly increasing their effective radii, their number density is also decreasing fast to be transformed into bulge+disk galaxies, which results in a decrease of the effective radius because of the mass going into the central parts of the galaxy to build the bulge. As a result, the two effects compensate to produce a flat size evolution. From $z \sim 1.5$, the morphological mixing remains roughly constant and the average growth simply reflects the growth of the different morphological types. Interestingly, all dominant morphologies (spheroids, disks, and disk+spheroids) at these redshifts do grow but the growth rate is different. While spheroids increase their effective radii by a factor of ~3 (~5 from $z \sim 3$), disks and disk+spheroids grow only by a factor of ~1.5. The latter is roughly consistent with the expected growth of disks in galaxy haloes, i.e., $R_e \propto H(z)^{-1}$ (black dashed–dotted lines in Figure 10), which comes from the theoretical assumption that disks are formed with a fixed fraction of mass and angular momentum of the parent halo (e.g., Mo et al. 1998; Ferguson et al. 2004). Spheroids grow at a faster rate as already pointed out by Huertas-Company et al. (2013) with a different selection, suggesting that some other mechanism takes place in these systems.

Sérsic indices also increase on average from $n \sim 1.5$ to $n \sim 4$, but again with different behaviors depending on morphology. The spheroids have $n > 3$ and they increase up to $n \sim 5$, confirming their bulge-dominated morphologies at all epochs. On the other hand, irregular disks have very low n values ($n \sim 1$) while disk and disk+spheroids have rather constant intermediate values (with $n \sim 1.5$ for disks and $n \sim 2.5-3$ for disk+sph). This also confirms the validity of our morphological classification. Considering all these trends, the average observed increase of the Sérsic index (black line in
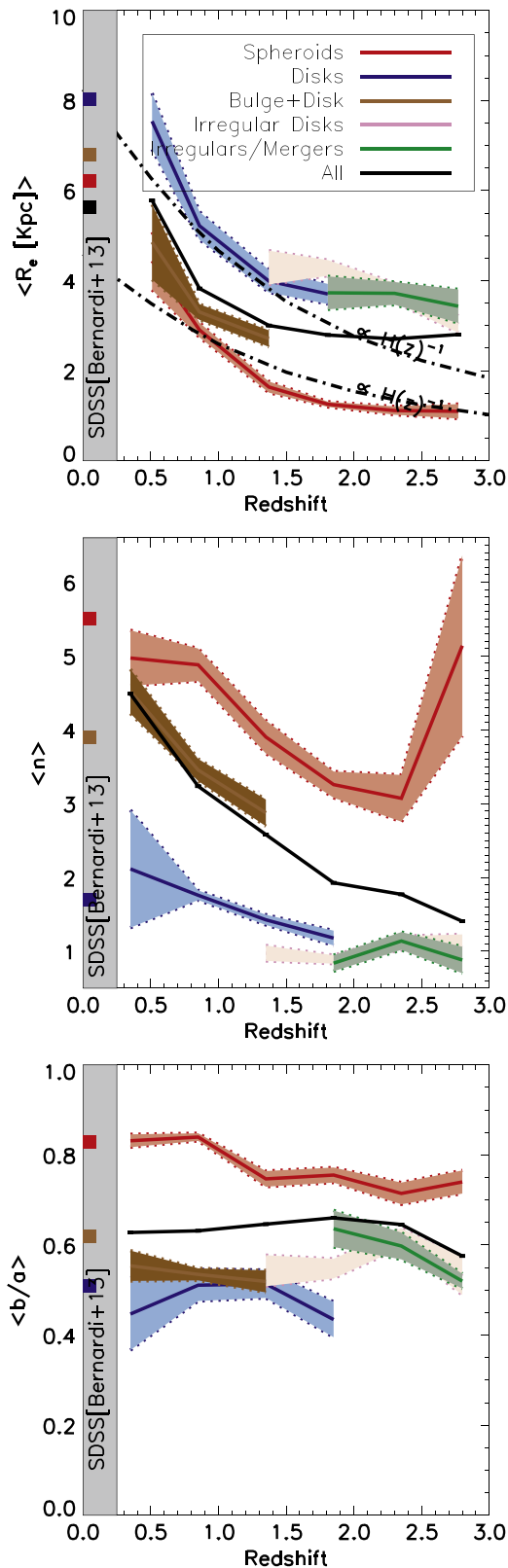
Figure 10. Evolution of the median effective radius (top panel), Sérsic index (middle panel), and axis ratio (bottom panel) for different morphologies. The red, brown, blue, magenta, and green lines show spheroids, bulge+disks, disks, irregular disks, and irregulars, respectively. The black line shows all galaxies irrespective of their morphology. Error bars are estimated through bootstrapping. The squares show the values at $z \sim 0$ from Bernardi et al. (2014) and the dashed–dotted black lines in the top panel show the relation $H(z)^{-1}$ normalized to the value for spheroids and disks at $z \sim 0.8$.

Figure 10) is again better explained as a combination of morphological transformations from clumpy disks to regular systems, which produces a growth of the bulge and an increase in the Sérsic index together with the *individual* increase of spheroids. The general increase of the Sérsic index is also observed by Shankar et al. (2015) and might help to explain part of the evolution in the lensing profile of early-type galaxies.

Axis ratios show little evolution with redshift but the absolute values change significantly with the morphological type. Spheroids have b/a values close to 0.8 while all the other morphological classes present values of $0.5 - 0.6$, which again suggests that there are two families of objects following different evolutions. The measured values are also in good agreement with measurements in the local universe for similar morphologies (Bernardi et al. 2013).

In Figure 11 we analyze the total mass density profiles for different morphologies. As also done in Patel et al. (2013), we compute the median mass density profile using the best-fit Sérsic models at different redshifts and convert them to stellar masses by normalizing by the stellar mass of each galaxy (see Shankar et al. 2013 for details). This procedure is clearly a first-order approximation since it neglects any gradient in the stellar populations that could definitely modify the shape of the profiles (especially for the star-forming galaxies). The figure clearly shows that spheroids are rapidly increasing their size at a faster rate than the average (bottom panel), with most of the action happening toward the galaxy outskirts through the addition of material. The central parts remain unaltered from $z \sim 3$ (changes in the inner 1 kpc would not be detected given the point-spread function size). The evolution of the mass density profile for disks and disk+spheroids is less dramatic, resulting in a milder increase of their size, but the changes happen also at radii larger than $3 - 4$ kpc. Interestingly, the clumpy disks do show a significant evolution of their profile, which could be interpreted as gas accretion happening in these objects and bringing material to the outskirts. These trends should, however, be taken with caution, especially for the star-forming population, since first we neglect any stellar population gradient by construction when building the stacked mass profiles and second the profiles are obtained through single-component fits that might not be well adapted to reproduce the irregular light distribution of clumpy galaxies.

7. DISCUSSION: TWO CHANNELS OF BULGE GROWTH

The results presented in the previous sections seem to indicate two different evolutionary tracks for massive galaxies $(\log(M_*/M_\odot) \sim 11.2 \pm 0.15)$ and for the growth of their bulge component which are summarized in Figure 12. As a matter of fact, the detailed analysis of the morphological properties of the progenitors from $z \sim 3$ shows that there are two distinct families of galaxies with different physical properties. Interestingly, a similar conclusion is reached by Cappellari et al. (2011) based on the kinematic study of nearby massive early-type galaxies.

7.1. The Nugget Track—Fast Assembly

About $\sim 30\%$ of massive galaxies had a spheroid morphology at $z \sim 2.5$—with no disk component—and this fraction does not evolve down to $z \sim 0$. The quiescent fraction for the
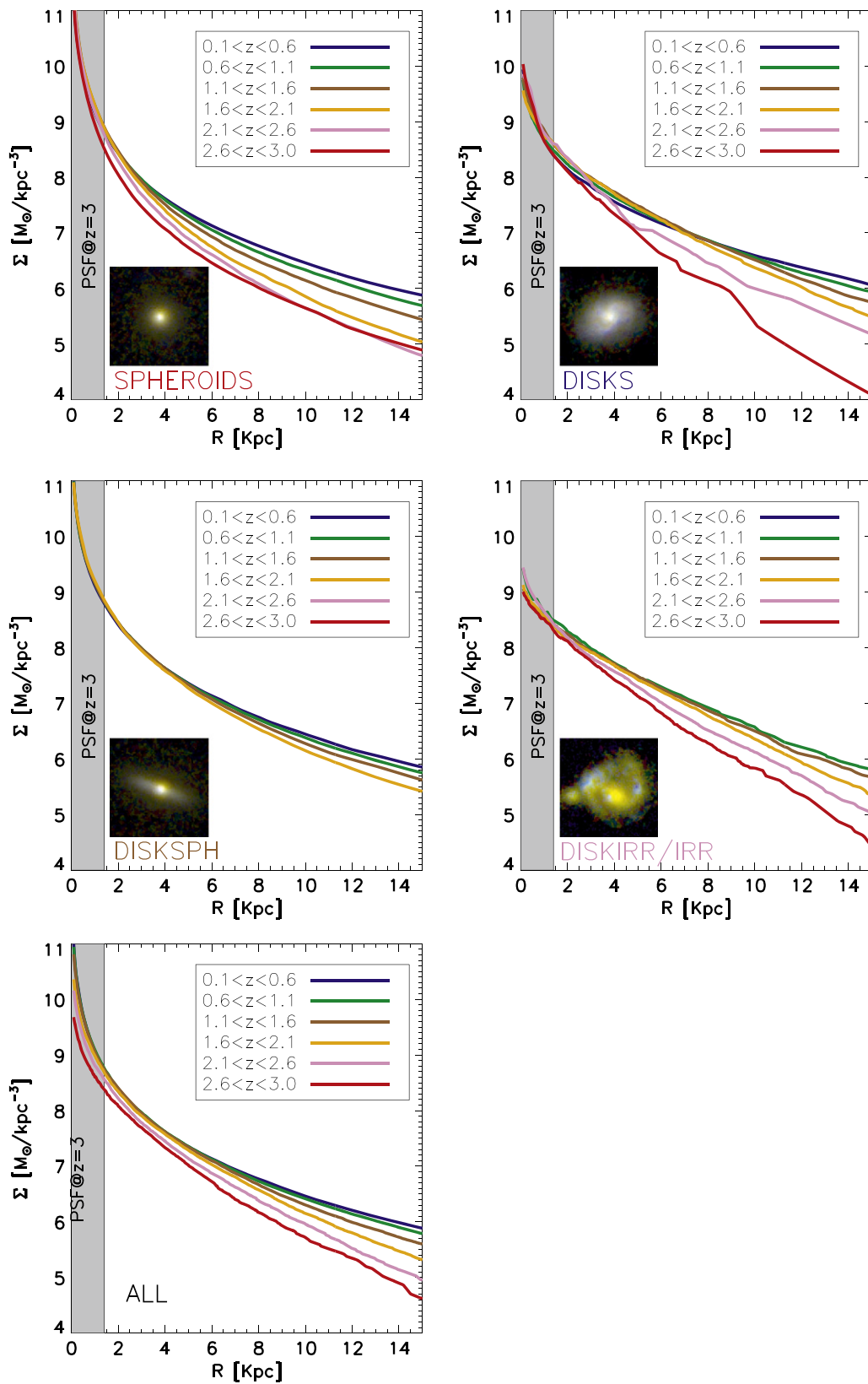
Figure 11. Median stellar mass density profiles for different morphologies in different redshift bins as labeled. The top left panel, top right panel, middle left panel, and middle right panel show the profiles for spheroids, disks, disk+spheroids, and irregular disks, respectively. The bottom panel shows the average profiles for all galaxies.
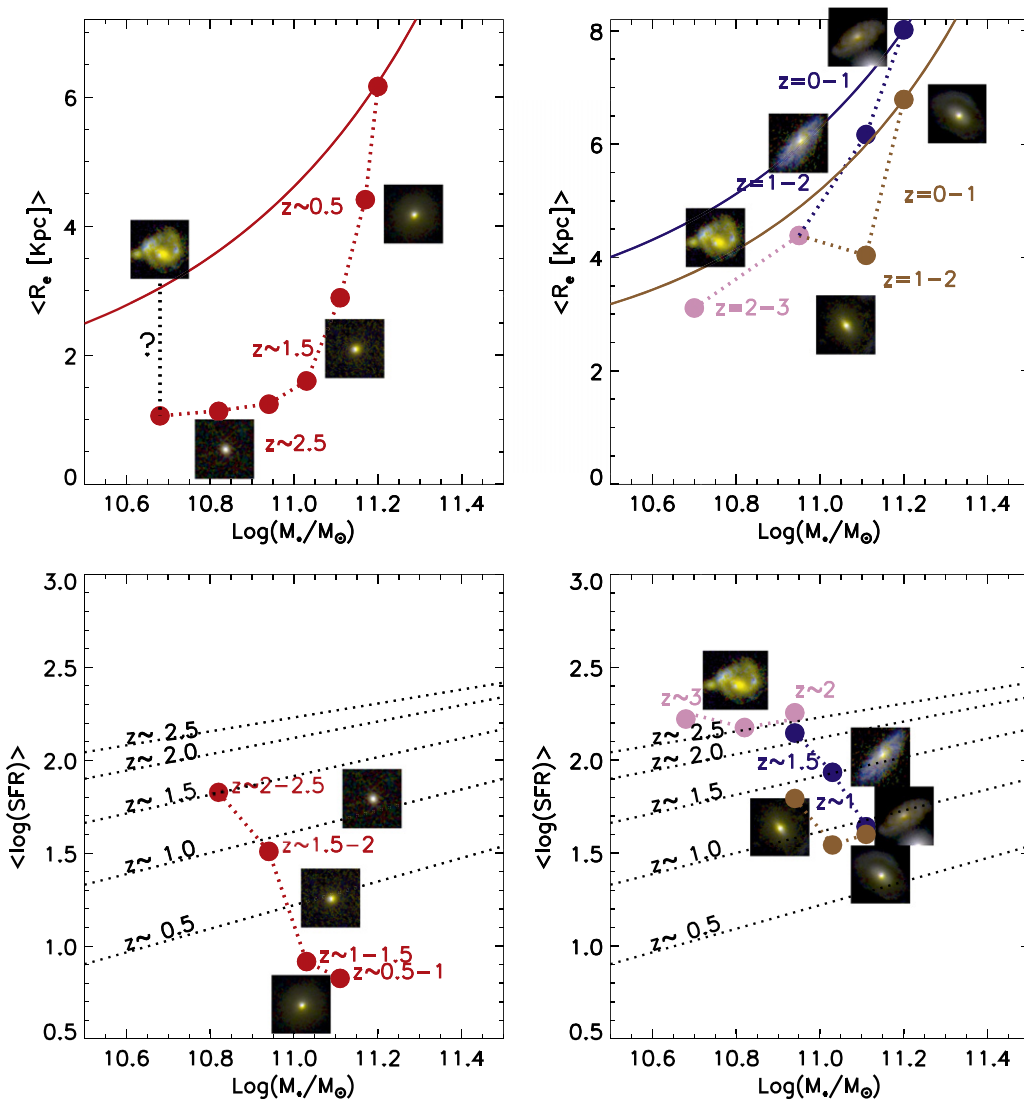
Figure 12. Expected evolution in the mass–size (top) and M_*–SFR (bottom) planes of the two channels of bulge growth (see text for details). The left panels show the evolution of spheroids. The right panels show the evolutionary track of clumpy disks. The red, brown, and blue solid lines in the top panels show the $z \sim 0$ median mass–size relation from Bernardi et al. (2014) for ellipticals, early spirals, and late spirals, respectively. The dashed lines in the bottom panels indicate the median star-forming main sequence at different redshifts from Whitaker et al. (2012).

spheroid population is also rather high ($\sim 50\%$), and their gas fraction is low ($\sim 10\%-15\%$) from $z \sim 2$ and increases between $z \sim 2-3$, which suggests that these galaxies are rapidly assembling at $z \sim 2.5$ and above. The fraction of passive spheroids rises to almost 100% at $z < 0.5$, indicating that they are in the process of quenching in the epoch probed by this work but without significant alterations of their morphologies, in agreement with the findings of Barro et al. (2013, 2014) and Mei et al. (2014) for dense regions. Their SFRs remain indeed well below the main sequence of star formation at all epochs (Figure 12). The fast quenching is also accompanied by a rapid growth of their effective radii by a factor of ~ 5, compared to a factor of 2 growth in stellar mass, with most of the action happening in the galaxy outskirts ($R > 4$ kpc). The Sérsic index also increases from $n \sim 3$ to $n \sim 5$, even though it remains rather high at all epochs, confirming their bulge-dominated morphology. They are therefore very similar to the dense-core galaxies identified by van Dokkum et al. (2014). The increase in the Sérsic index, however, is not coupled to the gas content, at variance with

what is observed for the average population (Papovich et al. 2014), which suggests an external driver. The fact that the number density and the morphologies do not change supports the idea that the reported growth is indeed an individual growth of these objects and that it is not driven by the morphological transformations or quenching of *new* galaxies (progenitor bias). Otherwise, we would expect an increase in their abundance, since it is very unlikely that these galaxies will transform into another morphological class (although this cannot be fully excluded as discussed in section 7.3). An independent test for this statement would be a detailed analysis of the stellar population ages for this particular population, which will be addressed in forthcoming work with higher resolution SEDs. Recall that the size growth is even larger than that measured for the overall population (i.e., a factor of 2–3), which is in fact a convolution of different mechanisms as described below. The properties of these galaxies are therefore consistent with the formation of the bulk of their stellar populations at high redshifts through violent disk instabilities or gas-rich mergers (at $z \sim 2.5$ their gas fraction is

high and also their sSFR) that created their dense cores (Kaviraj et al. 2013; Barro et al. 2014; Dekel & Burkert 2014), and a subsequent growth by the addition of material in the outskirts through, possibly, minor mergers. Figure 12 summarizes the inferred evolution of these objects in the mass–size and M_*–SFR planes from $z \sim 3$. It is worth emphasizing that the size growth for these objects at later epochs ($z < 1$) is still very pronounced, i.e., a factor of ~ 2 with a minimum stellar mass growth. The global trend is nevertheless still compatible, at first order, with a growth driven by minor mergers, as predicted by numerical and semi-empirical models (e.g., Shankar et al. 2015 for slightly larger stellar masses). However, a more detailed comparison with the models' predictions is required at this stage.

7.2. The Clumpy Track—Slow Assembly

The remaining $\sim 60\%$ of the population is made of irregular/clumpy disks at $z \sim 3$ which experience a rapid morphological transformation between $z = 3$ and $z = 1$ to give birth to very massive disks with a small bulge ($\sim 20\%$) and to 40% of galaxies with both a prominent bulge and a disk component. The evolution of the effective radii is more moderate than for spheroids and scales roughly with $H(z)^{-1}$, the expected growth of disks in DM haloes. Figure 12 summarizes the inferred evolution of these objects in the mass–size and M_*–SFR planes from $z \sim 3$. The transition from the clumpy-irregular morphologies to more Hubble sequence-like galaxies happens mostly at $z > 1$. Clumpy-irregular disks are characterized by high SFRs ($>100 M_\odot$ yr^{-1}, slightly above the main sequence at that epoch), high gas fractions ($\sim 60\%$), and low Sérsic indices ($n \sim 1$). Some of these objects ($\sim 1/3$) will experience a smooth transition to become massive spirals with low bulge/total (B/T) fractions. As a matter of fact, the properties of both families are very similar, in terms of gas fractions, Sérsic index, SFRs, and also effective radii. The other $\sim 2/3$ will build a more prominent bulge ($n > 2.5$), which roughly corresponds to B/T of 50%–75% (Bruce et al. 2012). The building-up of a larger bulge component results in a decrease of the effective radius following the concentration of mass toward the central regions. The emergence of the bulge is also tightly correlated with the decrease of the star formation activity and the decrease of the gas fractions, which go from 50% to $\sim 10\%$, making them depart from the star formation main sequence (Figure 12). This evolution is consistent with the predictions of several numerical simulations (e.g., Martig et al. 2009; Bournaud 2015) that show how the growth of a bulge through clump migration is followed by a decrease of the star formation activity (*morphological quenching*) although the effect of feedback from a SMBH in the growing bulge could also produce similar effects. As a matter of fact, active galactic nucleus feedback is known to contribute to the quenching of star formation (e.g., Silk & Rees 1998; Granato et al. 2004) and it is also known to correlate with the mass of the bulge (e.g., Kormendy & Ho 2013), and therefore it could also help to explain the quenching of bulge+disk systems, which seems to be associated with the growth of the bulge.

7.3. Major Mergers

This two-track scenario is obviously not the only possible explanation for the trends we observe. Namely, the constant number of spheroids could also be a result of clumpy gas-rich galaxies being transformed into spheroids following a major merger event and spheroids regrowing a disk at the same rate (e.g., Hammer et al. 2009; Hopkins et al. 2009). Since the inferred gas fractions of irregular systems are high ($\sim 40\%$), this is a plausible option. The scenario requires, however, a fine-tuning to keep these two effects (formation of spheroids and disk regrowth) at the same rate and also a high (major) merger fraction to keep producing spheroids. There have been several measurements of the major merger rate (1:4) of massive galaxies ($M_*/M_\odot \sim 10^{11}$) in the recent literature. From the observational point of view, Lotz et al. (2011) measure 1.6 mergers/galaxy between $z \sim 0$–3 (extrapolating the quoted redshift evolution). This is in rather good agreement with Man et al. (2012), who find 1.1 mergers/galaxy in the same period, and also with López-Sanjuan et al. (2012). Bluck et al. (2009, 2012) find a larger fraction (1.7 mergers/galaxy only between $z = 1.7$ and $z = 3$). Abundance matching-based measurements (e.g., Hopkins et al. 2010) also find similar numbers (1.7 mergers/galaxy between $z = 0$ and $z = 3$), just like semi-analytical models (e.g., Conselice et al. 2014) and numerical simulations (e.g., Kaviraj et al. 2014). In this work we use the model of Behroozi et al. (2013), which predicts 1.2 major mergers/galaxy along the mass growth track shown in Figure 2.

Considering these different measurements, it is certainly safe to assume that, on average, each galaxy in our sample experiences a major merger event in the redshift range explored. Assuming then that each merger event is enough to change the morphology, it is indeed possible to explain the decrease in number density of irregular disks by mergers followed by disk rebuilding. We notice, however, that the simulations of Hopkins et al. (2009) focusing on disk rebuilding predict that only equal-mass mergers are able to create bulge-dominated systems. Mergers with lower mass ratios (1:2–1:4) tend to create disk-dominated systems that continue forming stars. In that respect, if mergers+disk rebuilding is the dominant channel, we would expect at all epochs an increasing fraction of star-forming regular disks and a minor fraction of quiescent bulge-dominated systems. The opposite is actually observed.

In addition to this, we do observe that the median ages of the spheroids in our sample estimated through SED fitting increase monotonically from ~ 0.5 Gyr at $z > 2$ to ~ 2.5 Gyr at $z \sim 0.5$ (roughly consistent with the time between these two redshift bins). On the other hand, the ages of disk-dominated systems tend to stay rather young (<1 Gyr) at all epochs due to the sustained star formation. If the dominant process to create the 30% spheroids we observe is merging, we would not expect the strong increase in the ages of spheroids that we actually seem to observe. Given the known degeneracies affecting age determination from broadband photometry, these trends need to be treated with caution. However, they point toward an early formation of the spheroid population. A further check of the proposed bulge growth tracks would therefore imply accurate age estimations of the bulge components in the different galaxy types. This requires bulge-to-disk decompositions and high-resolution SED fitting of the different components, which is ongoing.

8. SUMMARY

We have analyzed the morphological, structural, and star formation properties of the progenitors of massive galaxies

$(M_*/M_\odot \sim 10^{11.2\pm0.3})$ from $z \sim 3$. The progenitors are selected using abundance matching to take into account the expected mass growth in the redshift range probed in this work. The latter selection is a key point of the present work and is clearly subjected to important assumptions (i.e., halo mass functions, galaxy SMFs, and halo occupation distribution functions) as explained in the previous sections. It is worth emphasizing, however, that selecting galaxies at fixed stellar mass (i.e., assuming the extreme scenario in which galaxies do not grow in mass) results in very similar trends to those reported here.

The main new ingredient of this work is the addition of accurate visual-like morphologies, which help us to better understand the different evolutionary tracks leading to the present-day Hubble sequence. We have defined five main morphological types that quantify the presence or lack of a bulge/disk component and the presence or absence of irregularities in the light profile. We then have explored the abundances, SFRs, quiescent fractions, gas fractions, and structural properties for each morphological type.

Our main results are the following:

1. The morphologies of massive galaxies significantly change from $z \sim 3$. At $z < 1$, these galaxies are consist of 40% pure spheroids, 40% bulge+disk galaxies (early spirals and lenticulars) and 20% massive disks. At $z \sim 3$ there is still 40% spheroids, but the remaining 60% is made up of irregular/clumpy disks or disturbed galaxies. Most of the morphological transformations take place at $z > 1$.

2. As reported in previous works, the overall population of massive galaxies rapidly quenches from $z \sim 3$ to $z \sim 0$, i.e., the quiescent fraction increases from $\sim20\%$ to $\sim80\%$, the median SFR decreases from $\sim100 M_\odot$ yr^{-1} to $\sim25 M_\odot$ yr^{-1}, and the gas fractions go from $\sim40\%$ to $\sim15\%$. When inspected at fixed visual morphology the trends are very different. The quiescent fraction in the spheroid population is already high at $z \sim 3$, i.e., 60%, and increases to almost 100%. The quiescent fraction for disks and disk irregulars remains low ($<20\%$) at all epochs while for bulge+disk objects the fraction appears to be constant too at a value of 40%–50%. These trends suggest that the overall increase in the quenching fraction for the whole population can be explained by a combination of the quenching of the spheroid population with the morphological transformation from clumpy/irregular disk to early spiral/S0.

3. When considering the overall population, without morphological distinction, we measure an increase in the average effective radius by a factor of 2–3 as well as an increase in the Sérsic index from $n \sim 1.5$ to $n \sim 4$, as reported in the recent literature for similar selections. The evolution of the average mass density profile is also in agreement with an inside-out growth. The evolution of the average size seems to have two different regimes: from $z \sim 3$ to $z \sim 1.5$, there is almost no significant change of the effective radius, while the bulk of the growth happens from $z \sim 1.5$ to $z \sim 0$. At fixed morphologies, spheroids do grow by a factor of $5-6$ from $z \sim 3$ and increase their Sérsic index from $n \sim 3$ to $n \sim 5$. On the other hand, irregular disks and disks grow by a factor of ~1.5 and keep a rather constant Sérsic index ($n < 2$ for disks and disk+irr and $n \sim 2.5-3$ for

disk+bulge galaxies). The two different phases in the average growth are better explained if morphological transformations are taken into account. In the first phase, there is a rapid morphological transformation from clumpy disks to bulge+disk galaxies which results in a slight decrease in the effective radius as a consequence of the mass concentration toward the inner regions of the galaxy. Even though spheroids and clumpy disks increase their size in this period, the rapid decrease in the number density of the latter seems to compensate this growth and results in no evolution of the average size. During the second phase, from $z \sim 1.5$, the morphological mixing remains roughly constant, but the size growth increases by a factor of $\sim2-3$ on average. This growth is therefore better explained by the individual growth of disk/disk+bulge galaxies, which grow by a factor of ~1.5, and the growth of the spheroids, which increase their effective radius by a factor of ~4.

The above results suggest two different channels for the bulge growth in the massive end of the Hubble sequence:

1. A *nugget* track (fast assembly) followed by 30%−40% of the population of massive galaxies. Galaxies created in that way formed the bulk of the stars at $z > 2.5$ and also acquired their spheroidal morphology at these early epochs, possibly through violent disk instabilities (and/or mergers) which rapidly bring gas into the central parts. At $z < 2$, they have already low gas fractions, low SFRs, and high Sérsic indices, and $\sim60\%$ of them are classified as quiescent. They are, however, very compact with median effective radii of ~5 kpc. Between $z \sim 3$ and $z \sim 0.5$ they almost completely stop forming stars while they increase their size by a factor of ~5 and their Sérsic index from $n \sim 3$ to $n \sim 5$, keeping their global visual aspect unaffected. The growth is decoupled from the gas content and the SFRs, which remain low at all epochs, and mostly happens in the galaxy outskirts, suggesting an ex situ driven growth.

2. A *clumpy* track (slow assembly) followed by 60%−70% of the population of massive galaxies at $z \sim 0$. These galaxies were clumpy/irregular star-forming disks (SFR $> 100 M_\odot$ yr^{-1}) at $z \sim 2-3$. From $z \sim 3$ to $z \sim 1$ they experience a rapid morphological transformation leading to relaxed systems (at least in terms of their visual aspect) and to the emergence of a bulge component of variable size ($\sim2/3$ seem to develop a large bulge component while the remaining 1/3 keep a disk-dominated morphology). The morphological transformation is accompanied by a decrease in the SFR (reaching $\sim50 M_\odot$ yr^{-1}) and the gas fraction (going down to $\sim15\%$), more dramatically for galaxies developing a larger bulge, as well as by an increase in the Sérsic index (from $n \sim 1$ to $n \sim 2.5-3$) and a decrease in the effective radius because of the mass being concentrated toward the inner regions. This is in good agreement with the predictions of numerical simulations in which the bulge component is built from the migration of clumps and the stabilization of the disk results in a decrease of the SFR (*morphological quenching*) although the possible effect of a SMBH should also be considered. Major merger events followed by a disk rebuilding event could also contribute to transforming irregular systems

but this is unlikely to be the dominant channel in the mass range explored in this paper. Below $z \sim 1$, the well-known massive end of the Hubble sequence is in place and the galaxy properties change only marginally. Their effective radii grow in fact at a rate roughly consistent with $H(z)^{-1}$, the expected growth due to the hierarchical assembly of haloes (e.g., Stringer et al. 2014).

REFERENCES

Baldry, I. K., Glazebrook, K., & Driver, S. P. 2008, MNRAS, 388, 945
Barro, G., Faber, S. M., Pérez-González, P. G., et al. 2013, ApJ, 765, 104
Barro, G., Faber, S. M., Pérez-González, P. G., et al. 2014, ApJ, 791, 52
Barro, G., Pérez-González, P. G., Gallego, J., et al. 2011a, ApJS, 193, 30
Barro, G., Pérez-González, P. G., Gallego, J., et al. 2011b, ApJS, 193, 13
Behroozi, P. S., Marchesini, D., Wechsler, R. H., et al. 2013, ApJL, 777, LL10
Behroozi, P. S., Wechsler, R. H., & Conroy, C. 2013, ApJ, 770, 57
Bell, E. F., Papovich, C., Wolf, C., et al. 2005, ApJ, 625, 23
Bernardi, M., Meert, A., Sheth, R. K., et al. 2013, MNRAS, 436, 697
Bernardi, M., Meert, A., Vikram, V., et al. 2014, MNRAS, 443, 874
Bernardi, M., Roche, N., Shankar, F., & Sheth, R. K. 2011, MNRAS, 412, L6
Bezanson, R., van Dokkum, P. G., Franx, M., et al. 2011, ApJL, 737, LL31
Bluck, A. F. L., Conselice, C. J., Bouwens, R. J., et al. 2009, MNRAS, 394, L51
Bluck, A. F. L., Conselice, C. J., Buitrago, F., et al. 2012, ApJ, 747, 34
Bournaud, F. 2015, arXiv:1503.07660
Bournaud, F., Perret, V., Renaud, F., et al. 2014, ApJ, 780, 57
Brammer, G. B., van Dokkum, P. G., & Coppi, P. 2008, ApJ, 686, 1503
Brammer, G. B., van Dokkum, P. G., Franx, M., et al. 2012, ApJS, 200, 13
Bruce, V. A., Dunlop, J. S., Cirasuolo, M., et al. 2012, MNRAS, 427, 1666
Bruzual, G., & Charlot, S. 2003, MNRAS, 344, 1000
Buitrago, F., Trujillo, I., Conselice, C. J., & Haeussler, B. 2011, MNRAS, 428, 1460
Buitrago, F., Trujillo, I., Conselice, C. J., et al. 2008, ApJL, 687, L61
Calzetti, D., Armus, L., Bohlin, R. C., et al. 2000, ApJ, 533, 682
Cappellari, M., Emsellem, E., Krajnović, D., et al. 2011, MNRAS, 416, 1680
Carollo, C. M., Bschorr, T. J., Renzini, A., et al. 2013, ApJ, 773, 112
Cassata, P., Giavalisco, M., Williams, C. C., et al. 2013, ApJ, 775, 106
Chabrier, G. 2003, PASP, 115, 763
Cimatti, A., Nipoti, C., & Cassata, P. 2012, MNRAS, 422, L62
Conselice, C. J., Bluck, A. F. L., Mortlock, A., Palamara, D., & Benson, A. J. 2014, MNRAS, 444, 1125
Conselice, C. J., Mortlock, A., Bluck, A. F. L., Grützbauch, R., & Duncan, K. 2013, MNRAS, 430, 1051
Daddi, E., Renzini, A., Pirzkal, N., et al. 2005, ApJ, 626, 680
Dahlen, T., Mobasher, B., Faber, S. M., et al. 2013, ApJ, 775, 93
Damjanov, I., Abraham, R. G., Glazebrook, K., et al. 2011, ApJL, 739, L44
Damjanov, I., Geller, M. J., Zahid, H. J., & Hwang, H. S. 2015, ApJ, 806, 158
Dekel, A., & Birnboim, Y. 2008, MNRAS, 383, 119
Dekel, A., & Burkert, A. 2014, MNRAS, 438, 1870
Ferguson, H. C., Dickinson, M., Giavalisco, M., et al. 2004, ApJL, 600, L107
Fukushima, K. 1980, Biological Cybernetics, 36, 193202
Galametz, A., Grazian, A., Fontana, A., et al. 2013, ApJS, 206, 10

Gehrels, N. 1986, ApJ, 303, 336
González, J. E., Lacey, C. G., Baugh, C. M., Frenk, C. S., & Benson, A. J. 2009, MNRAS, 397, 1254
Granato, G. L., De Zotti, G., Silva, L., Bressan, A., & Danese, L. 2004, ApJ, 600, 580
Grogin, N. A., Kocevski, D. D., Faber, S. M., et al. 2011, ApJS, 197, 35
Guo, Y., Ferguson, H. C., Giavalisco, M., et al. 2013, ApJS, 207, 24
Hammer, F., Flores, H., Puech, M., et al. 2009, A&A, 507, 1313
Hopkins, P. F., Cox, T. J., Younger, J. D., & Hernquist, L. 2009, ApJ, 691, 1168
Hopkins, P. F., Croton, D., Bundy, K., et al. 2010, ApJ, 724, 915
Huertas-Company, M., Mei, S., Shankar, F., et al. 2013, MNRAS, 428, 1715
Ilbert, O., McCracken, H. J., Le Fèvre, O., et al. 2013, A&A, 556, AA55
Kartaltepe, J. S., Mozena, M., Kocevski, D., et al. 2014, arXiv:1401.2455
Kaviraj, S., Cohen, S., Ellis, R. S., et al. 2013, MNRAS, 428, 925
Kaviraj, S., Devriendt, J., Dubois, Y., et al. 2014, arXiv:1411.2595
Kennicutt, R. C., Jr. 1998, ApJ, 498, 541
Koekemoer, A. M., Faber, S. M., Ferguson, H. C., et al. 2011, ApJS, 197, 36
Kormendy, J., & Ho, L. C. 2013, ARA&A, 51, 511
Kriek, M., van Dokkum, P. G., Franx, M., Illingworth, G. D., & Magee, D. K. 2009, ApJL, 705, L71
Lapi, A., González-Nuevo, J., Fan, L., et al. 2011, ApJ, 742, 24
Leja, J., van Dokkum, P., & Franx, M. 2013, ApJ, 766, 33
López-Sanjuan, C., Balcells, M., Pérez-González, P. G., et al. 2010, A&A, 518, AA20
Lotz, J. M., Jonsson, P., Cox, T. J., et al. 2011, ApJ, 742, 103
Man, A. W. S., Toft, S., Zirm, A. W., Wuyts, S., & van der Wel, A. 2012, ApJ, 744, 85
Marchesini, D., Muzzin, A., Stefanon, M., et al. 2014, ApJ, 794, 65
Marchesini, D., van Dokkum, P. G., Förster Schreiber, N. M., et al. 2009, ApJ, 701, 1765
Marchesini, D., Whitaker, K. E., Brammer, G., et al. 2010, ApJ, 725, 1277
Martig, M., Bournaud, F., Teyssier, R., & Dekel, A. 2009, ApJ, 707, 250
Mei, S., Holden, B. P., Blakeslee, J. P., et al. 2009, ApJ, 690, 42
Mei, S., Scarlata, C., Pentericci, L., et al. 2014, arXiv:1403.7524
Mo, H. J., Mao, S., & White, S. D. M. 1998, MNRAS, 295, 319
Mortlock, A., Conselice, C. J., Bluck, A. F. L., et al. 2011, MNRAS, 413, 2845
Mortlock, A., Conselice, C. J., Hartley, W. G., et al. 2013, MNRAS, 433, 1185
Moster, B. P., Naab, T., & White, S. D. M. 2013, MNRAS, 428, 3121
Moustakas, J., Coil, A. L., Aird, J., et al. 2013, ApJ, 767, 50
Mundy, C. J., Conselice, C. J., & Ownsworth, J. R. 2015, MNRAS, 450, 3696
Muzzin, A., Marchesini, D., Stefanon, M., et al. 2013, ApJ, 777, 18
Naab, T., Johansson, P. H., & Ostriker, J. P. 2009, ApJL, 699, L178
Newman, A. B., Ellis, R. S., Bundy, K., & Treu, T. 2012, ApJ, 746, 162
Nipoti, C., Treu, T., Leauthaud, A., et al. 2012, MNRAS, 422, 1714
Oser, L., Ostriker, J. P., Naab, T., Johansson, P. H., & Burkert, A. 2010, ApJ, 725, 2312
Papovich, C., Labbé, I., Quadri, R., et al. 2014, ApJ, 803, 26
Patel, S. G., van Dokkum, P. G., Franx, M., et al. 2013, ApJ, 766, 15
Peng, C. Y., Ho, L. C., Impey, C. D., & Rix, H.-W. 2002, AJ, 124, 266
Peng, Y.-J., Lilly, S. J., Kovač, K., et al. 2010, ApJ, 721, 193
Pérez-González, P. G., Rieke, G. H., Villar, V., et al. 2008, ApJ, 675, 234
Poggianti, B. M., Moretti, A., Calvi, R., et al. 2013, ApJ, 777, 125
Schmidt, M. 1959, ApJ, 129, 243
Shankar, F., Buchan, S., Rettura, A., et al. 2015, ApJ, 802, 73
Shankar, F., Guo, H., Bouillot, V., et al. 2014, ApJL, 797, LL27
Shankar, F., Marulli, F., Bernardi, M., et al. 2013, MNRAS, 428, 109
Shen, S., Mo, H. J., White, S. D. M., et al. 2003, MNRAS, 343, 978
Silk, J., & Rees, M. J. 1998, A&A, 331, L1
Sonnenfeld, A., Nipoti, C., & Treu, T. 2014, ApJ, 786, 89
Stringer, M. J., Shankar, F., Novak, G. S., et al. 2014, MNRAS, 441, 1570
Trujillo, I., Ferreras, I., & de La Rosa, I. G. 2011, MNRAS, 415, 3903
Trujillo, I., Förster Schreiber, N. M., Rudnick, G., et al. 2006, ApJ, 650, 18
Valentinuzzi, T., Poggianti, B. M., Saglia, R. P., et al. 2010, ApJL, 721, L19
van der Wel, A., Bell, E. F., Häussler, B., et al. 2012, ApJS, 203, 24
van der Wel, A., Franx, M., van Dokkum, P. G., et al. 2014, ApJ, 788, 28
van der Wel, A., Holden, B. P., Zirm, A. W., et al. 2008, ApJ, 688, 48
van Dokkum, P. G., Bezanson, R., van der Wel, A., et al. 2014, ApJ, 791, 45
van Dokkum, P. G., Brammer, G., Fumagalli, M., et al. 2011, ApJL, 743, L15
van Dokkum, P. G., Franx, M., Kriek, M., et al. 2008, ApJL, 677, L5
van Dokkum, P. G., Whitaker, K. E., Brammer, G., et al. 2010, ApJ, 709, 1018
Whitaker, K. E., van Dokkum, P. G., Brammer, G., & Franx, M. 2012, ApJL, 754, LL29
Wuyts, S., Förster Schreiber, N. M., Genzel, R., et al. 2012, ApJ, 753, 114
Wuyts, S., Förster Schreiber, N. M., van der Wel, A., et al. 2011, ApJ, 742, 96